HYDROTHERMAL PERFORMANCE ANALYSIS AND MULTI-OBJECTIVE OPTIMIZATION OF MICROCHANNEL 3D-IC WITH ALTERNATING SECONDARY FLOW CHANNELS

***Pinzhong CHEN*[a] *and Zhongliang PAN*[a*]**

[a] School of Electronics and Information Engineering, South China Normal University, Foshan, China

[*] Corresponding author; E-mail: panzhongliang@m.scnu.edu.cn

Embedding microchannels in a 3D-IC can alleviate heat dissipation problems. In this paper, microchannel 3D-IC with alternating secondary flow channel was proposed and geometric parameters were optimized. Non-dominated Sorting Genetic Algorithm II was used for Pareto optimization. Optimization solutions (R_{t_best}, P_{p_best} and ψ_{best}) were selected in Pareto front. The optimization objective values of these solutions are all less than the corresponding values of conventional design. Based on Pareto front, a compromise solution for Technique for Order Preference by Similarity to an Ideal Solution was calculated. Compared with conventional design, the thermal resistance of R_{t_best}, pumping power of P_{p_best}, and chip uniformity index of ψ_{best} are reduced by 10.2%, 3.4% and 7.3%, respectively. Compared with conventional design, the thermal resistance, pumping power, and chip uniformity index of compromise solution based on Technique for Order Preference by Similarity to an Ideal Solution are reduced by 10.0%, 1.0% and 7.1%, respectively. The results may help the development of optimization design of the microchannel in 3D-IC.

Key words*: 3D-IC, microchannel, alternating secondary flow channel, hydrothermal performance, multi-objective programming*

1. Introduction

As an emerging technology, three-dimensional integrated circuit (3D-IC) is gradually changing traditional integrated circuit design concepts. Compared with traditional two-dimensional chip, 3D-IC stacks multiple chip layers and vertically interconnects them through through-silicon-via (TSV), which can fully utilize vertical space and achieve higher integration, smaller interconnect length, and faster data transmission speed [1-3]. The emergence of this technology not only meets the demands of modern electronic devices for high performance, miniaturization and low power consumption, but also brings new opportunities for the development of the integrated circuit industry. However, with the continuous improvement of 3D-IC integration, its heat dissipation problem is becoming increasingly prominent [4-7]. Due to the high integration of the chip, heat accumulates inside the chip. If not dissipated in a timely manner, it will reduce the performance of the chip and shorten its service life [8-10]. Therefore, how to effectively alleviate the heat dissipation problem of 3D-IC has become one of the current research hotspots. As a device with excellent heat dissipation effect, microchannels have broad application prospects for microelectronic devices that require high cooling performance [11].

Microchannels contain tiny fluid channels that can achieve rapid heat transfer and effective dissipation within the chip [12, 13]. When the cooling fluid flows through the microchannel, it takes away the heat inside the chip, thereby reducing the temperature of the chip. Tuckerman and Pease pioneered the concept of microchannel cooling, effectively utilizing it for IC temperature reduction [14]. They achieved a remarkable cooling potential of 790 W/cm2 by etching microchannels into silicon substrates, using water as the cooling agent. Following this breakthrough, the microchannel heat sink garnered significant interest for its space-saving design and exceptional cooling performance. Li et al. research examined five degrees of freedom heat sink configurations within a hybrid heat sink featuring microchannel fins integrated into 3D-IC [15]. The results indicate that a fin cross section characterized by a greater width and length, along with an inward contraction or the creation of ribs on all four sides, can lead to lower maximum and mean temperatures within the heat sink. Wang et al. conducted optimization research on the length to width ratio of rectangular single fins and staggered fins, as well as the columnar distance between fins, in hybrid microchannel heat sinks for a series of specific objectives [16]. He et al. investigated the thermoelectric coupling effect of TSV integrated micro pin fins in 3D-IC and found that the extended fins exhibited the best overall heat transfer performance at an angle of 30 degrees [17]. Yan et al. investigated the positive effect of enhancing microfluidic cooling by fin-shaped pin-fin and found that different structures of fin-shaped pin-fin will have influence on the separation point of flow [18]. Zhang et al. established a rectangular parallel phase change microchannel model in a 3D electronic device with R134a as the cooling fluid [19]. The overall performance was enhanced by reducing the inlet temperature of cooling fluid and microchannel number appropriately. Zhang et al. designed an embedded microchannel heat sink with TSV etched micro pin fins, which was optimized through steady-state and transient simulations and improved in heat dissipation capacity and mechanical reliability compared with the 2.5-D package [20]. Huang et al. analyzed the combined effects of filling mode and rib arrangement on flow and heat transfer characteristics and found that microchannel incompletely filled with aligned ribs exhibited the best overall performance when Reynolds number is 400 [21].

The characteristics of secondary flow channel is that alternating slanted secondary channels are used to form secondary flow in the microchannel and enhance heat transfer performance. There is research on microchannel heat sinks related to alternating secondary flow channels currently [22]. However, there is no investigation on combining microchannel 3D-IC with alternating secondary flow channels. The structure of 3D-IC and the non-uniformity distribution of heat sources have influence on heat transfer and flow characteristics.

Microchannel 3D-IC based on alternating secondary flow channels is proposed in this paper. In order to analyze and optimize the performance of the model, the number, inclination angle and width of secondary flow channels are used as design variables. Thermal resistance, pumping power and chip uniformity index are used as optimization objectives. Using Non-dominated Sorting Genetic Algorithm II, the Pareto front was obtained. When the thermal resistance, pumping power and chip uniformity index are minimized, different optimization solutions can be selected from the Pareto front. In order to obtain the best compromise solution, the optimization result based on Technique for Order Preference by Similarity to an Ideal Solution was calculated.

2. Numerical simulation methods

2.1. Geometric model

Fig. 1 (a) shows the geometric model of the microchannel 3D-IC proposed in this paper. The model includes processor layer, wiring layer (a film of silicon dioxide), memory layer and microchannel region. Each four prism in the microchannel region is a micro pin fin. In microchannel 3D-IC, micro pin fins are also considered as TSVs, which are used to establish communication between process layer and wiring layer. Deionized water is used as a cooling fluid and flows in microchannel regions to enhance heat dissipation. Solid materials (Si and SiO2) were used in this model, and SiO2 is the material of the wiring layer. The physical properties such as density, specific heat and thermal conductivity of deionized water, Si and SiO2 were set based on the build-in material library of COMSOL. In order to reduce the computational complexity of the physical field in microchannel 3D-IC, periodic boundary conditions were used to simplify the model to the region enclosed by the red wireframe in Fig. 1 (a). More details are shown in Fig. 1 (b), (c), and (d). The heat flux in the gray region (core region) in Fig. 1 (b) is approximately 5 times that of the white region (surrounding region), which results in a larger temperature difference in the processor layer for multi-core 3D-IC [23]. Fig. 1 (c) is the top view of the secondary flow channel, where Nc represents dividing the microchannel in Fig. 1 (b) into Nc equal parts in the y-direction. Placing a smaller secondary channel at an angle between the main channels can induce secondary flow to move from one main channel to another through the secondary channel. Alternating arrangements can form secondary flow with alternating directions from the main channel to another main channel. In addition, the area of the isosceles trapezoid in the middle of Fig. 1 (c) is equal to the sum of the areas of the trapezoids on both sides. More detailed information related to the geometric parameters in Fig. 1 is shown in Tab. 1.

Table 1. Geometric parameters of microchannel 3D-IC

Parameter	Variable	Dimension
Microchannel 3D-IC length	L	10 mm
Microchannel 3D-IC width	W	10 mm
Microchannel 3D-IC height	H	0.41 mm
Core region length	L_c	2.5 mm
Surrounding region length	L_s	2.5 mm
Number of cycles	N_p	2, 3, …, 20
Acute angle of isosceles trapezoid	θ	27.76°~45°
Secondary flow channel width	W_s	0.1~0.2 mm
Processor layer height	H_p	0.1 mm
Microchannel height	H_c	0.2 mm
Wiring layer height	H_w	0.01 mm
Memory layer height	H_m	0.1 mm
Microchannel width	W_c	0.1 mm
Micro pin fin width	W_f	0.1 mm

2.2. Governing equations and boundary conditions

Some assumptions are used to simplify the hydrothermal analysis of microchannel 3D-IC. Firstly, the flow is laminar and steady. Secondly, the fluid is single-phase and incompressible. Thirdly, natural convection heat transfer and thermal radiation is ignored. Governing equations are as follows:

Continuity equation:

$$\rho\nabla\cdot\vec{V}=0$$

Momentum equation:

$$\rho(\vec{V}\cdot\nabla)\vec{V}=-\nabla P+\nabla(\mu\nabla\vec{V})$$

Energy equation of fluid domain:

$$\rho C_{\mathrm{p}}\vec{V}\cdot\nabla T-\nabla(k\nabla T)=0$$

Energy equation of solid domain:

$$\nabla(k\nabla T)=0$$

where ρ denotes density; $\vec{V}$ represents speed; P represents pressure; μ indicates dynamic viscosity; C_{p} represents specific heat; T represents temperature; k represents heat transfer coefficient.

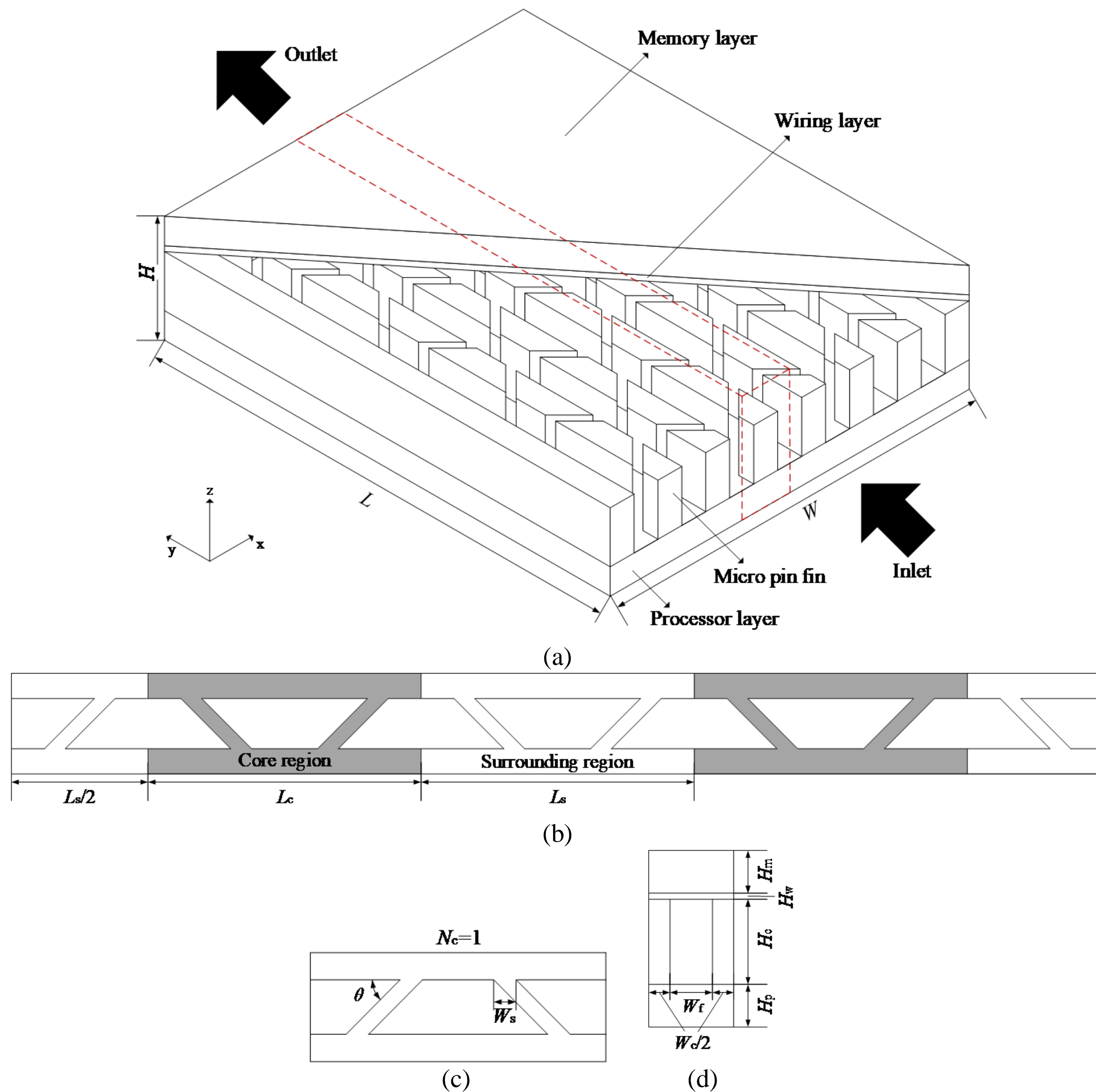

Figure. 1 (a) Microchannel 3D-IC with alternating secondary flow channels, (b) microchannel region with periodic boundary condition, (c) top view of microchannel when Nc = 1, (d) front view.

COMSOL Multiphysics simulation software was used to calculate temperature, velocity, and pressure. For the boundary conditions, the temperature and mass flow rate of the fluid at the inlet of the microchannel are set to 293.15 K and 4 × 10-5 kg/s, respectively. In order to investigate the effects of multi-cores on microchannel 3D-IC, the heat fluxes of core regions and surrounding regions were set at the bottom of the model to 1.7 × 106 W/m2 and 3.4 × 105 W/m2, respectively. A heating condition of 105 W/m2 was set at the top of the memory layer. The solid surfaces of the inlet and outlet are set to be adiabatic. The cooling fluid velocity at the solid-liquid interface is set to be no slip, and the temperature on this surface is continuous.

2.3. Performance indices

In this paper, three parameters (R_t, P_P, and ψ) were used to measure hydrothermal performance. The thermal resistance R_t is related to temperature, and the specific relationship formula is as follows [24]:

$$R_t = \frac{T_{c,max} - T_{f,min}}{Q_c + Q_s} \tag{1}$$

where $T_{c,max}$ represents the maximum temperature in the core regions; $T_{f,min}$ represents the minimum temperature of the fluid; Q_c represents the dissipated power in the core regions; Q_s represents the dissipated power in the surrounding regions.

The pumping power P_p is given by [25]:

$$P_p = \frac{N_m m_m \Delta P}{\rho_f} \tag{2}$$

where N_m represents the number of microchannels; m_m represents the fluid mass flow rate at the inlet; ΔP represents the pressure drop of the microchannel; ρ_f represents the density of the fluid at the inlet

Increasing the temperature gradient will increase thermal stress. Therefore, an index is used to evaluate the effect of various designs on chip temperature uniformity. Chip temperature uniformity index ψ is defined as follows [26]:

$$\psi = \frac{q_s}{q_c}\left(T_{c,max} - T_{s,min}\right) \tag{3}$$

where q_c represents the heat flux in the core regions; q_s represents the heat flux in the surrounding regions; $T_{s,min}$ represents the minimum temperature in the surrounding regions.

2.4. Numerical grid

The physical domain is mainly divided into memory layer, wiring layer, microchannel and processor layer. The shapes of memory layer, wiring layer, and microchannel are regular in the z-axis direction. Hexahedra were used for meshing. The bottom of the processor layer is set with non-uniform heat flux and free tetrahedrons were used for meshing in the processor layer. A grid independence verification was performed using four different grid numbers (4.4, 7.2, 11.5 and 17.3 million under non-periodic boundary condition). When the grid number increased from 7.2 to 11.5 million, the variations of R_t, P_P, and ψ were 2.4%, 2.7%, and 1.0%, respectively. An overly dense grid division may significantly increase the calculation time. Therefore, a grid size of 7.2 million was used to obtain reliable simulation results.

3. Optimization for geometric parameters

By establishing an agency model, the results of numerical calculations can be fitted to obtain objective functions, which is helpful for subsequent multi-objective programming problem. When there are too many design variables, it is difficult to accurately obtain the agency model through simple linear regression or polynomial regression. Radial Basis Function (RBF) neural network has a simple structure and is adept at handling nonlinear regression problems. In order to obtain more accurate optimal solutions, optimization problems were discussed from the perspective of multi-objective programming (MOP). N_c, θ and W_s are used to represent design variables; R_t, P_P and ψ are used to represent optimization objectives. The mathematical model can be mathematically formulated as:

$$\min R_t = f(N_c, \theta, W_s)$$
$$\min P_p = f(N_c, \theta, W_s)$$
$$\min \psi = f(N_c, \theta, W_s)$$

s.t.

$$2 \le N_c \le 20, \text{and } N_c \in \mathrm{Z}$$
$$27.76° \le \theta \le 45°$$
$$0.1\,mm \le W_s \le 0.2\,mm$$
$$\frac{100}{\tan\theta} + W_s < \frac{5000}{N_c} \tag{4}$$

where Z represents a set of integers. It is worth noting that N_c, θ and W_s are mutually constrained. For example, after selecting a smaller θ and a larger W_s, only a smaller N_c can be selected. The objective function ($f(N_c, \theta, W_s)$) is obtained through agency model based on RBF neural network. Therefore, the key to the multi-objective programming problem in this paper is how to obtain the optimal solution. Non-dominated Sorting Genetic Algorithm II (NSGA2) is a multi-objective evolutionary algorithm. It is based on the framework of genetic algorithm and is effective in solving multi-objective problems. Due to the need to minimize all optimization objectives, fitness functions of NSGA2 in this paper are equal to objective functions. The NSGA2 algorithm flow is shown in Fig. 2.

When performing crossover or mutation, it is necessary to consider four constraints on the design variables. When assigning parameters, the population size, number of iterations, crossover probability, and mutation probability were set to 100, 150, 0.7, and 0.4, respectively. The process of non-dominated sorting is concise. There are two sufficient conditions for the fitness of the i-th population to be higher than that of the j-th population: $\boldsymbol{Y}_{si} \leqslant \boldsymbol{Y}_{sj}, \forall s \in \{1,2,\ldots,S\}$; $\boldsymbol{Y}_{si} < \boldsymbol{Y}_{sj}, \exists s \in \{1,2,\ldots,S\}$. Y is the optimization objective matrix. The number of optimization objectives S is discrete and the range of values for s can only be integers.

4. Results and discussion

The diagram of Pareto front can intuitively show the distribution of the optimized set and the relationship between various optimization objectives. The relationship between the three optimization objectives is shown in Fig. 3 (a), (b), and (c). It can be seen that the Pareto front distribution of R_t and ψ tends to a straight line with a positive slope, indicating that ψ can also be taken near the minimum value when R_t is taken near the minimum value. From Fig. 3 (a) and (c), it can be observed that there is a negative correlation between P_p and R_t, as well as a negative correlation between P_p and ψ. In

other words, R_t and ψ inevitably increase as P_p decreases. One of the reasons is that when the overall flow velocity of the microchannel decreases due to the adjustment of design variable values, it can reduce P_p but decrease the performance of thermal convection, leading to an increase in R_t and ψ. In addition, in Fig. 3 (a), when P_p = 0.052-0.054, two unsmoothed points appear continuously at the Pareto front. One reason for this phenomenon is that N_c can only take discrete values.

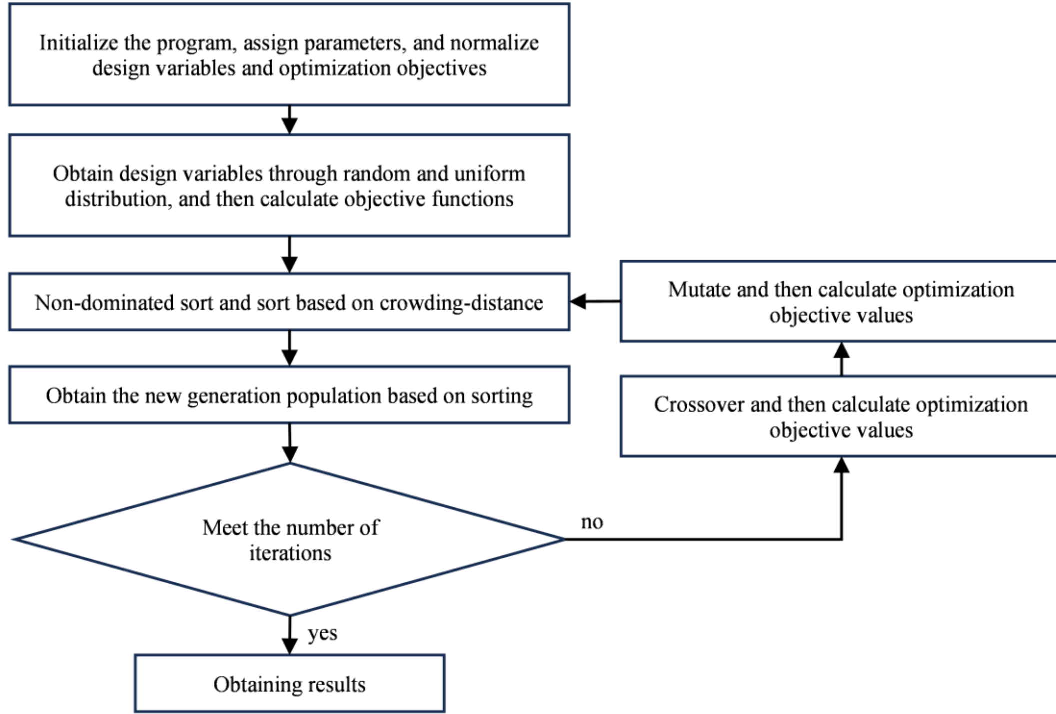

Figure. 2 Algorithm flow based on NSGA

Conventional design represents the microchannel without secondary flow channels. The simulation software COMSOL is used to obtain the results of conventional design. In many papers, the results of conventional design are compared with those of optimized microchannel structures to evaluate the hydrothermal performance of the proposed microchannels [27-29]. Therefore, a comparison is made between microchannel 3D-IC based on conventional design and microchannel 3D-IC with alternative secondary flow channel proposed in this paper in terms of hydrothermal performance. When the optimization objectives R_t, P_p, and ψ are obtained based on the Pareto front, the corresponding result distribution is shown in Fig. 4. Pareto front in the figure represents the Pareto front calculated using NSGA2; partial Pareto front represents the part of the Pareto front that is completely superior to the results of conventional design; R_{t_min}, P_{p_min}, and ψ_{min} represent the results corresponding to the minimum values of R_t, P_p, and ψ of the Pareto front. It can be seen that only the values of R_t, P_p, and ψ corresponding to partial solutions (solutions corresponding to partial Pareto front) of the Pareto front are less than those corresponding to conventional design. In other words, the microchannel with secondary flow channels needs to have reasonable parameter settings in order to achieve completely better hydrothermal performance than conventional design. The minimum values of R_t, P_p, and ψ are 11.7%, 8.4%, and 9.5% less than those of conventional design, respectively. However, the fitness of the solutions (R_{t_min}, P_{p_min}, and ψ_{min}) and the fitness of the conventional design are the same. These solutions do not overlap with the partial Pareto front, indicating that when the

minimum value of R_t, P_p, or ψ is taken, the values corresponding to other optimization objectives are larger than those of conventional design results.

In order to obtain the optimal value under the circumstance that the Pareto front fitness is higher than the conventional design fitness, further analysis is necessary. For the Pareto optimal solution obtained in this paper, selecting the relative optimal solution from the Pareto optimal solution is a typical Multi-attribute Decision Making (MADM) problem. Technique for Order Preference by Similarity to an Ideal Solution (TOPSIS) method can be used to handle this problem. In addition to the best compromise solution of TOPSIS, we have selected solutions based on Pareto front that is completely superior to conventional design hydrothermal performance. The minimum values of R_t, P_p, and ψ in the selected solutions were calculated to obtain R_{t_best}, P_{p_best} and ψ_{best}.

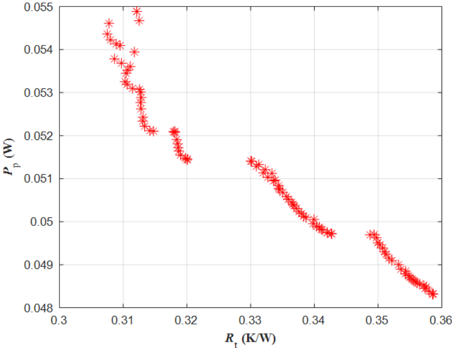

(a)

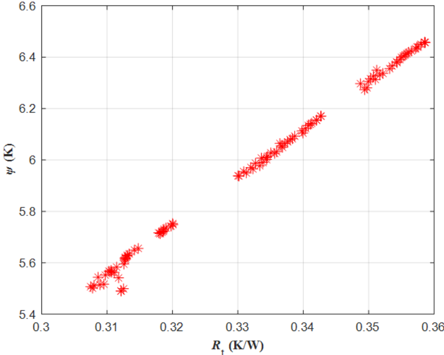

(b)

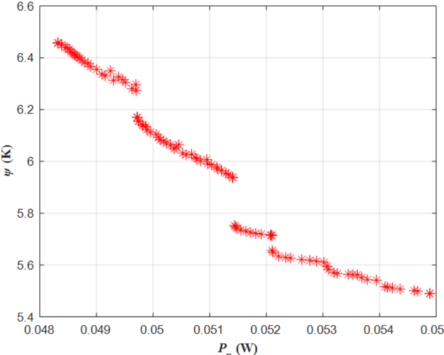

(c)

Figure. 3 Diagram for Pareto front

When the mass flow rate is 4×10^{-5} kg/s and z = 200 μm, the temperature distribution corresponding to various solutions is shown in Fig. 5. The characteristic of conventional design is that

the highest temperature value in the solid domain is larger and the area of the high-temperature region is the largest. In addition, the temperature of fluid away from the solid domain at the outlet (left side of the microchannel) is lower, indicating that the heat transfer efficiency of the fluid in this region is lower. For Pp_min, the number of micro pin fins is the largest; the width of secondary flow channels is larger; the θ value is larger. These parameter settings can all increase the volume of the fluid domain in the microchannel. The characteristic of P_{p_min} is that the volume of the fluid domain is the largest and the pumping power value is the smallest. However, the value of the highest temperature in P_{p_min} is close to the value of the highest temperature in conventional design. In addition, the setting of P_{p_min} increases the fluid temperature of secondary flow channels in the high-temperature region. In other words, these secondary flow channels have lower work efficiency. The θ value of R_{t_min} and ψ_{min} are both smaller, which facilitates fluid flow between secondary flow channels and main channels and reduces the highest temperature value in the red high-temperature region (Fig. 5) compared with P_{p_min}. It is worth noting that the N_c value of ψmin is significantly smaller than that of R_{t_min}. The smaller the N_c value, the larger the volume of the solid domain in the microchannel. A larger solid domain of ψ_{min} can make the temperature more uniform. However, the area of red high-temperature region of ψ_{min} is larger than that of R_{t_min}, indicating that the average temperature of ψ_{min} is higher and the smaller N_c makes the high-temperature region distribution approach that of conventional design. To balance R_t, P_p, and ψ, it is necessary to obtain compromise solutions for N_c, θ, and W_s. The geometric parameter settings for R_{t_best}, ψ_{best}, and P_{p_best} are similar. Compared with R_{t_best} and ψ_{best}, the N_c value corresponding to TOPSIS remains unchanged but θ and W_s are slightly adjusted. The design variables and optimization objectives corresponding to conventional design and optimization solutions (R_{t_best}, P_{p_best}, ψ_{best} and TOPSIS) are shown in Tab. 2.

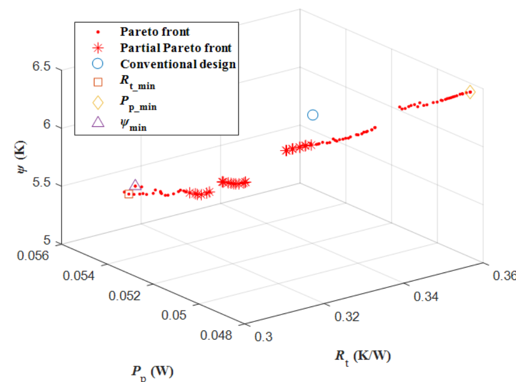

Figure. 4 Comparison of Pareto optimization and conventional design

It can be seen in Tab. 2 that the values of optimization objectives in TOPSIS are all smaller than the values corresponding to conventional design. It is worth noting that the Pp weight of TOPSIS is the smallest compared with R_t and ψ. Therefore, the P_p value of TOPSIS is larger and only 1.0% lower than the P_p value of conventional design. However, for R_t and ψ, TOPSIS values are 10.0% and 7.1% smaller than conventional design values, respectively. The solutions of R_{t_best} and ψ_{best} are the same, with their R_t and ψ being respectively 10.2% and 7.3% smaller than those of conventional design but the optimization percentage of P_p is 0%. P_{p_best} has a smaller optimization percentage. For P_{p_best}, the optimization percentages of R_t, P_p, and ψ are 4.2%, 3.4%, and 1.2%, respectively. Overall, the optimization of R_t is evident for all solutions.

Table 2 Design variable values and optimization objective values for optimization solutions

	N_c	θ (°)	W_s (μm)	R_t (K/W)	P_p (W)	ψ (K)
R_{t_best}	11	27.87	191.7	0.3128	0.05262	5.622
P_{p_best}	14	32.61	189.8	0.3338	0.05097	5.990
ψ_{best}	11	27.87	191.7	0.3128	0.05262	5.622
TOPSIS	11	27.93	196.4	0.3134	0.05222	5.634
Conventional design	-	-	-	0.3483	0.05276	6.064

In order to evaluate the accuracy of the MOP method in this paper, numerical simulations were conducted using the geometric parameters of optimization solutions. Tab. 3 shows the results of MOP methods and numerical simulations. By comparison, the maximum error is 0.9%. Therefore, the predicted values obtained using the agency model in Pareto optimization have good predictive accuracy.

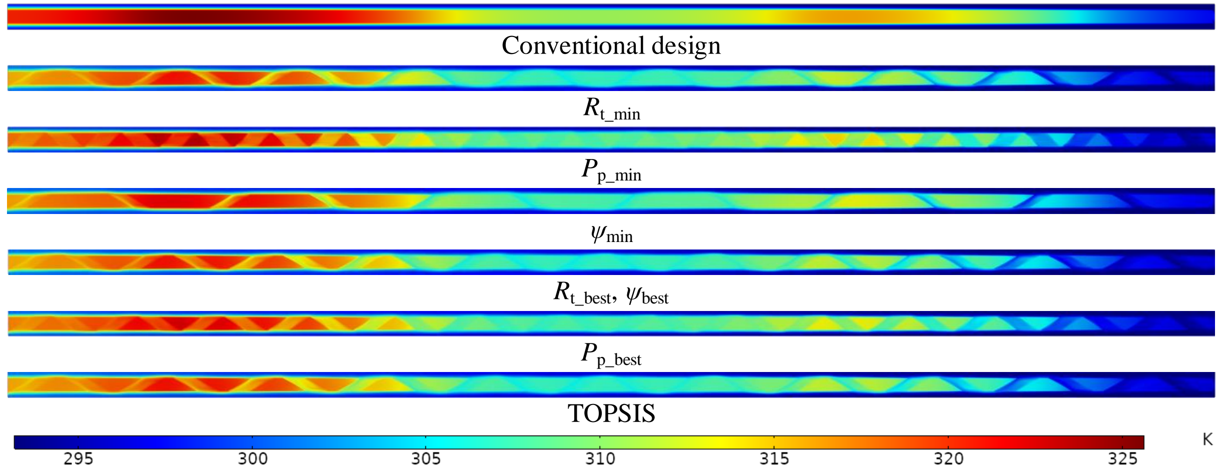

Figure. 5 Temperature distributions of conventional design and optimization solutions

Table 3 Comparison of MOP results and numerical values

	Optimization objective						δ (%)		
	MOP value			Numerical value					
	R_t	P_p	ψ	R_t	P_p	ψ	R_t	P_p	ψ
R_{t_best}	0.3128	0.05262	5.622	0.3104	0.05227	5.588	0.8	0.7	0.6
P_{p_best}	0.3338	0.05097	5.990	0.3325	0.05050	5.962	0.4	0.9	0.5
ψ_{best}	0.3128	0.05262	5.622	0.3104	0.05227	5.588	0.8	0.7	0.6
TOPSIS	0.3134	0.05222	5.634	0.3106	0.05186	5.595	0.9	0.7	0.7

5. Conclusions

In this paper, microchannel 3D-IC with alternating secondary flow channels is proposed. The characteristic of this model is that secondary flow channels are designed in the microchannel and the heat flux in the processor layer is nonuniform. The design variables are the number, oblique angle and

width of secondary flow channels. The optimization objectives are thermal resistance, pumping power and chip uniformity index. For MOP problems, the NSGA2 algorithm was used to obtain Pareto front and optimization solutions. Based on Pareto front, TOPSIS solution and other compromise solutions were calculated. Pareto front was obtained using NSGA2. The tendency of Pareto front for R_t and ψ is a straight line with a positive slope. P_p and R_t are negatively correlated and P_p and ψ are also negatively correlated, which indicates that the optimal solution is difficult to make the values of R_t and ψ minimum while obtaining the minimum value of P_p. The minimum values of R_t, P_p and ψ based on Pareto front are 11.7%, 8.4%, and 9.5% less than those of conventional design, respectively. However, according to the definition of non-dominated sorting in NSGA2, these solutions cannot be completely superior to conventional design. The optimization objective values of TOPSIS, R_{t_best}, P_{p_best}, and ψ_{best} are all less than the values corresponding to conventional design. The values of R_t, P_p and ψ of TOPSIS are 10.0%, 1.0%, and 7.1% less than the corresponding values of conventional design, respectively. The values of R_t and ψ of R_{t_best} are 10.2% and 7.3% less than the corresponding values of conventional design, respectively. The value of P_p of P_{p_best} is 3.4% less than the corresponding value of conventional design. This optimization method provides the engineering reference for the optimization design of geometric parameters of microchannel 3D-IC. Due to the fact that 3D-IC is multi-layered and has TSV, hydrothermal performance of multi-layer microchannel 3D-IC with TSV should be further investigated.

References

[1] D. Zhou, Y. Chen, W. Gao, et al., A novel thermal management scheme of 3D-IC based on loop heat pipe, *Int. J. Therm. Sci.*, 199 (2024), 108906

[2] U.K. Alugoju, S.K. Dubey, A. Javed, Optimization of converging and diverging microchannel heat sink for electronic chip cooling, *IEEE Trans. Comp., Packag. Manufact. Technol.*, 10 (2020), 5, pp. 817-827

[3] L. Gong, Y. P. Xu, B. Ding, et al., Thermal management and structural parameters optimization of MCM-BGA 3D package model, *Int. J. Therm. Sci.*, 147 (2020), pp. 106-120

[4] L. Ao, A. Ramiere, Through-chip microchannels for three-dimensional integrated circuits cooling, *Therm. Sci. Eng. Prog.*, 47 (2024), 102333

[5] S.S. Salvi, A. Jain, A review of recent research on heat transfer in three-dimensional integrated circuits (3-D ICs), *IEEE Trans. Compon. Packag. Manuf. Technol.*, 11 (2021), 5, pp. 802-821

[6] T. Liu, M.T. Dunham, K.W. Jung, et al., Characterization and thermal modeling of a miniature silicon vapor chamber for die-level heat redistribution, *Int. J. Heat Mass Transfer*, 152 (2020), 119569

[7] D. Medhat, M. Dessouky, D. Khalil, A programmable checker for automated 2.5D/3D IC latch-up verification and hot junctions detection, *Microelectron. Reliab.*, 124 (2021), 1, pp. 1-12

[8] S.J. Gräfner, J.H. Huang, V. Renganathan, et al., Fluidic-chemical characteristics of electroless copper deposition of ordered mass-fabricated pillars in a microchannel for chip packaging applications, *Chem. Eng. Sci.*, 269 (2023), 118474

[9] S. Kim, J. Seo, J. Choi, et al., Vertically Integrated Electronics: New Opportunities from Emerging Materials and Devices, *Nano Micro Lett.*, 14 (2022), 201

[10] X. Zhang, Z. Ji, J. Wang, et al., Research progress on structural optimization design of microchannel heat sinks applied to electronic devices, *Appl. Therm. Eng.*, 235 (2023), 121294

[11] Z.H. Wu, Z.Y. Jiang, W.J. Yan, et al., Jet microchannel with sawtooth wall for efficient cooling of high-power electronics, *Int. J. Heat Mass Transfer*, 206 (2023), 123955

[12] L. Zheng, Y. Zhang, G. Huang, et al., Novel electrical and fluidic microbumps for silicon interposer and 3D-ICs, *IEEE Trans. Compon. Packag. Manuf. Technol.*, 4 (2014), 5, pp. 777-785

[13] E. Bayrak, A.B. Olcay, M.F. Serincan, Numerical investigation of the effects of geometric structure of microchannel heat sink on flow characteristics and heat transfer performance, *Int. J. Therm. Sci.*, 135 (2019), pp. 589-600

[14] D.B. Tuckerman and R.F.W. Pease, High-performance heat sinking for VLSI, *IEEE Electron Device Lett.*, 2 (1981), 5, pp. 126-129

[15] Z.Q. Lu, Z.H. Xie, K. Xi, et al., Constructal evolutionary design of liquid cooling heat sink embedded in 3D-IC based on deep neural network prediction, *Int. Commun. Heat Mass Transfer*, 152 (2024), 107273

[16] R. Wang, Z.H. Xie, Z.Q. Lu, Second law constructal designs of hybrid single-finned and stagger-finned microchannel heat sinks, *J. Enhanced Heat Transfer*, 29 (2022), 4, pp. 115-142

[17] W. He, Z.X. Wang, J.Q. Li, et al., Investigation of heat transfer performance for through-silicon via embedded in micro pin fins in 3D integrated chips, *Int. Commun. Heat Mass Transfer*, 214 (2023), 124442

[18] Y.F. Yan, T. Zhao, Z.Q. He, Numerical investigation on the characteristics of flow and heat transfer enhancement by micro pin-fin array heat sink with fin-shaped strips, *Chem. Eng. Process. Process Intensif.*, 160 (2021), 108273

[19] J. Zhang, H. Feng, L. Chen, et al., Constructal design of a rectangular parallel phase change microchannel in a three-dimensional electronic device, *Sci. China Technol. Sci.*, 66 (2023), 12, pp. 3355–3368

[20] P. Zhang, D.W. Wang, W.S. Zhao, Investigation on Embedded Microchannel Heatsink for 2.5-D Integrated Package, *IEEE Trans. Compon. Packag. Manuf. Technol.*, 13 (2023), 6, pp. 838-848

[21] B.H. Huang, C. Mi, L. Gong, et al., Thermal management for multi-cores chips through microchannels completely or incompletely filled with ribs, *Case Stud. Therm. Eng.*, 54 (2024), 103977

[22] N.R. Kuppusamy, R. Saidur, N.N.N. Ghazali, et al., Numerical study of thermal enhancement in micro channel heat sink with secondary flow, *Int. J. Heat Mass Transfer*, 78 (2014), pp. 216-223

[23] A. Shakouri, Y. Zhang, On-chip solid-state cooling for integrated circuits using thinfilm microrefrigerators, *IEEE Trans. Compon. Packag. Manuf. Technol.*, 28 (2005), 1, pp. 65-69

[24] N. Tran, Y.J. Chang, J.T. Teng, et al., Enhancement thermodynamic performance of microchannel heat sink by using a novel multi-nozzle structure, *Int. J. Heat Mass Transfer*, 101 (2016), pp. 656-666

[25] X.J. Shi, S. Li, Y.J. Mu, et al., Geometry parameters optimization for a microchannel heat sink with secondary flow channel, *Int. Commun. Heat Mass Transfer*, 104 (2019), pp. 89-100

[26] A.R. Gharaibeh, M.I. Tradat, S. Rangarajan, et al., Multi-objective optimization of 3D printed liquid cooled heat sink with guide vanes for targeting hotspots in high heat flux electronics, *Int. J. Heat Mass Transfer*, 184 (2022), 122287

[27] C. Gao, X. Lan, Z. He, et al., Temperature uniformity analysis and multi-objective optimization of a small-scale variable density alternating obliquely truncated microchannel, *Therm. Sci. Eng. Prog.*, 38 (2023), 101652

[28] F. Zhang, B. Wu, B. Du, Heat transfer optimization based on finned microchannel heat sink, *Int. J. Therm. Sci.*, 172 (2022), 107357

[29] M. Pan, H. Wang, Y. Zhong, et al., Experimental investigation of the heat transfer performance of microchannel heat exchangers with fan-shaped cavities, Int. J. *Heat Mass Tran.*, 134 (2019), pp. 1199-1208

Submitted: 05.10.2024
Revised: 18.11.2024
Accepted: 27.11.2024